PCCP

Dissociation of the FEBID precursor cis-Pt(CO)2Cl2 driven by low-energy electrons

Journal:	*Physical Chemistry Chemical Physics*
Manuscript ID	CP-ART-12-2019-006633.R2
Article Type:	Paper
Date Submitted by the Author:	25-Jan-2020
Complete List of Authors:	Ferreira da Silva, Filipe; CEFITEC - Centre od Physics and Technological Research, Physics Department FCT/UNL Thorman, Rachel ; University of Iceland, Chemistry Bjornsson, Ragnar; University of Iceland Science Institute, Chemistry; Max-Planck-Institut für Chemische Energiekonversion Lu, Hang; University of Florida, Chemistry McElwee-White, Lisa ; University of Florida, Department of Chemistry Ingólfsson, Oddur; University of Iceland, Chemistry

ARTICLE

Dissociation of the FEBID precursor *cis*-$Pt(CO)_2Cl_2$ driven by low-energy electrons

Received 00th January 20xx,
Accepted 00th January 20xx

DOI: 10.1039/x0xx00000x

Filipe Ferreira da Silva,*[a] Rachel M. Thorman, [b] Ragnar Bjornsson, [b, c] Hang Lu, [d] Lisa McElwee-White[d] and Oddur Ingólfsson *[b]

In this study, we present experimental and theoretical results on dissociative electron attachment and dissociative ionisation for the potential FEBID precursor *cis*-$Pt(CO)_2Cl_2$. UHV surface studies have shown that high purity platinum deposits can be obtained from *cis*-$Pt(CO)_2Cl_2$. The efficiency and energetics of ligand removal through these processes are discussed and experimental appearance energies are compared to calculated thermochemical thresholds. The present results demonstrate the potential effectiveness of electron-induced reactions in the deposition of this FEBID precursor, and these are discussed in conjunction with surface science studies on this precursor and the design of the new FEBID precursors.

Introduction

For optimal exploitation of nanotechnology in the fabrication of functional nanostructures, it is essential to have fabrication methods that are flexible and capable of creating free-standing three-dimensional structures. Focused electron beam induced deposition (FEBID) is an emerging nanoscale direct writing technique with this capability and thus with potential to be complementary to the current lithographic approaches[1–3]. In FEBID, a high-energy electron beam (1-30 keV), typically in high-vacuum instrumentation (scanning- or transmission electron microscope), is focused onto a surface. Volatile precursor molecules are dosed continuously into the vacuum chamber, preferably in close proximity to the high-energy electron impact site at the surface. The high-energy electrons impinging on the surface undergo inelastic and elastic scattering, with a substantial contribution of inelastic ionizing scattering, leading to a considerable flux of low-energy secondary electrons along the primary electron tracks. These low-energy electrons interact with the precursor molecules at the substrate surface, leading to their decomposition and deposition of the nonvolatile fragments while volatile fragments are pumped away. Lateral control is achieved by moving the electron beam on the surface and high aspect ratio structures may be created by variation of the dwell time. In this manner, practically any shape can be fabricated on both flat and uneven surfaces. This capability, along with the "one-step" nature of this technique, provides the basis for its complementarity to current lithographic methods.

For the creation of metallic deposits, volatile organometallic precursors are typically used. Ideally, these precursors will decompose fully under the area of the primary electron beam, leaving the metal on the surface while the volatile ligands dissociate and desorb from the surface. Such complete decomposition is critical for the application of FEBID in the fabrication of functional nanostructures, where well-defined properties such as magnetism or conductivity may be essential. Currently used FEBID precursors typically do not meet the requirement of complete loss of ligand material - the metal content of deposits from organometallic FEBID precursors is generally low (< 50%)[1]. In recent years, there has been a concerted effort to improve this situation by better understanding the low-energy electron-induced chemistry leading to the formation of the deposits and to translate this understanding to design of better-performing FEBID precursors. In this context, a number of gas phase studies on low-energy electron interaction with current or potential FEBID precursors have been conducted[4–20], and many of the same precursors have been studied on surfaces under ultra-high vacuum (UHV) conditions[21,22 and refs. therein]. The combination of these approaches has given a good picture of the decomposition mechanisms for several precursors[21 and refs. therein]. Further, to better understand the fundamental steps in the deposition processes, a recent study has applied reflection absorption infrared spectroscopy and electron stimulated desorption to study the fundamental steps in Electron Beam Induced Surface Activation of the Metal-Organic Framework HKUST-1 in order to elucidate the underlying chemistry [23].

In principle, the decomposition of these precursors through interactions with low-energy secondary electrons may proceed through dissociative electron attachment (DEA), neutral- or dipolar dissociation (ND or DD) or dissociative ionization (DI). These are mechanistically different processes with different

[a] CEFITEC, Departamento de Física, Faculdade de Ciências e Tecnologia, Universidade NOVA de Lisboa, 2829-516 Caparica, Portugal
[b] Department of Chemistry and Science Institute, University of Iceland, Dunhagi 3,IS-107, Reykjavik, Iceland
[c] Department of Inorganic Spectroscopy, Max-Planck-Institut für Chemische Energiekonversion, Stiftstrasse 34-36, 45470 Mülheim an der Ruhr, Germany
[d] Univ Florida, Dept Chem, Gainesville, FL 32611-7200 USA

energy dependences and different products[22,24]. Furthermore, the relative efficiency of these processes will critically depend on the molecular structure of the precursor, offering a potential route to favourably direct the secondary electron-induced decomposition of FEBID precursors through rational design of their ligand set[25–27].

The first gas phase studies on low-energy electron interaction with FEBID precursor molecules were absolute measurements of the dissociation cross sections for $Co(CO)_3NO$ through DEA and DI[15,28] and absolute cross section measurements for DEA and electronic excitation for $Pt(PF_3)_4$ [4,19]. The gas phase cross sections for all of these processes were found to be exceptionally high. The decomposition of both molecules was also studied at surfaces irradiated with 500 eV primary electrons under controlled UHV conditions[29,30]. In the surface experiments, desorbing material was monitored by mass spectrometry while the evolution of the surface composition was monitored by X-ray photoelectron spectroscopy.

Similarly, gas phase studies on DEA and DI of $CpMePtMe_3$[14] were conducted in the context of earlier studies on the decomposition of this compound at surfaces[31,32].

For $Pt(PF_3)_4$ and $CpMePtMe_3$ in the gas phase, fairly extensive decomposition is observed in DI. Conversely, single ligand loss dominates the DEA process, which correlates well with surface experiments where single ligand loss was observed to be the dominant process for both of these compounds. This was taken as an indication that DEA dominated the initial step in the electron induced decomposition of these compounds at surfaces. We note, however, the cross sections for electronic excitation for $Pt(PF_3)_4$ were found to be very high and these electronically excited states were later shown in a theoretical study to be predominantly dissociative. The role of neutral dissociation may thus also be significant.

The comparison between the gas phase and surface studies on $Co(CO)_3NO$ was not as conclusive. However, as is the case for other heteroleptic carbonyl complexes, including $(\eta^3\text{-}C_3H_5)Ru(CO)_3Br$[33,34] and $CpFe(CO)_2Mn(CO)_5$[35,36], CO loss is the most efficient channel in gas phase DEA and DI of $Co(CO)_3NO$[15] and is also the initial decomposition step at surfaces[15].

From the experiments described above, electron-induced decomposition of other FEBID precursors, and the actual performance (deposit composition) of these precursors in FEBID, some deductions may be made as to which ligands are suitable for FEBID precursors. While alkyl and aryl ligands do not readily dissociate from the metal, carbonyl ligands appear to be more suitable leaving groups. Furthermore, due to their high electron affinity, halide ligands might be suitable leaving groups in DEA and/or might be removed from the initial deposit through further electron irradiation as was observed in the surface studies for $(\eta^3\text{-}C_3H_5)Ru(CO)_3Br$[37] and $Pt(CO)_2Cl_2$[38].

This notion was recently tested with a potential FEBID precursor, $(\eta^3\text{-}C_3H_5)Ru(CO)_3Br$ (and the corresponding chloride complex)[39]. This precursor combines the apparently persistent allyl ligand with the more easily removable carbonyl ligand and a halide. Surface studies[37] have shown effective CO loss in the initial electron-induced reaction of this precursor while the allyl group and the halogen were retained in the deposit. Further electron exposure of the deposit then led to slow, but effective halogen removal. A recent FEBID and post-deposition purification study[34] on this precursor shows an initial deposit with a Ru content of 23 at% that rises to about 80 at% after reductive post-deposition annealing with forming gas (2% H_2 / 98% N_2) at 300 °C. In this study, nearly complete oxygen loss is observed and the carbon content is reduced from the initial Ru:C ratio of 1:6 to 1:2. This is interpreted as the result of essentially complete CO loss and partial allyl loss. These surface and deposition studies are both qualitatively consistent with the complementary gas phase studies[39], where CO loss is the dominant channel in both DEA and DI.

In this context, *cis*-$Pt(CO)_2Cl_2$ is of interest because it contains only carbonyl and halogen ligands. Furthermore, surface studies show that when few monolayers of the surface-adsorbed compound is exposed to 500 eV electrons, the initial deposition step constitutes efficient carbonyl loss without significant halogen loss. Extended exposure of the initial deposit to electron irradiation leads to nearly quantitative chlorine desorption, leaving an almost pure Pt deposit. Consistent with that observation, deposition of *cis*-$Pt(CO)_2Cl_2$ under quasi-steady state conditions at room temperature leads to a $PtCl_2$ deposit with no noticeable CO remains. In the current contribution we report gas phase DEA and DI studies of *cis*-$Pt(CO)_2Cl_2$, and we compare the branching ratios of the observed DEA and DI channels to the results from a recent surface study[38].

Experimental Section

Experimental Set-up

Dissociative electron attachment and dissociative ionization processes were studied by means of a crossed electron-molecular beam apparatus[40]. In brief, an effusive molecular beam was generated by sublimation of *cis*-$Pt(CO)_2Cl_2$, via heating of the reservoir and inlet system to 85 ˚C. The interior of the vacuum chamber was maintained at 120 ˚C with internal halogen lamps. Heating the chamber served to prevent sample deposition on the ion extraction and trochoidal electron monochromator (TEM) electric lens components. The precursor was delivered under an argon atmosphere and transferred into the reservoir under a nitrogen atmosphere in a glove box. The inlet system was constructed of a 9 mm, capped Swagelok T-fitting separated from the chamber by a quarter turn plug valve. After placing the sample in the reservoir of the T fitting and an initial evacuation with a rough pump, the valve was carefully opened. This resulted in a sharp initial pressure rise in the chamber, which dropped gradually to a stable pressure of 1–2×10^{-5} Pa. This pressure was stable throughout the measurements as long as a sample was present. The background pressure of the collision chamber was approximately 1×10^{-6} Pa when no sample was introduced. Inside the chamber, the effusive sample beam entered the interaction zone through a stainless steel capillary, where it crossed a well-defined electron beam generated with a TEM[40]. The electron energy was calibrated to the well-known 0 eV

resonance for SF_6^- formation from SF_6[41] and the energy resolution was estimated from the full width at half maximum (FWHM) of the SF_6^- ion yield through this resonance. The electron energy resolution for the present measurements was around 110 meV. Fragment ions were measured with a Hiden EPIC1000 quadrupole mass spectrometer (Hiden Analytical, Warrington UK) equipped with an RF generator operating within a 2–1000 *m/z*-range.

$Pt(CO)_2Cl_2$ Synthesis

This compound was prepared by a modification of a literature procedure[42], in which PtI_2 (0.4 g, 0.9 mmol) was suspended in toluene (15 mL) in a Schlenk flask under N_2. After bubbling CO

$$PtI_2 + SO_2Cl_2 \xrightarrow[\text{toluene}]{\text{CO}} cis\text{-}Pt(CO)_2Cl_2$$

into the suspension for 2 hours, SO_2Cl_2 (0.6 g, 4.5 mmol) was added into the system and the reaction mixture was stirred at room temperature under N_2 for another 6 hours. During this time, the previously black suspension became a dark purple solution. Then, anhydrous *n*-heptane (30 mL) was added into the solution. Pale white crystals were obtained after storing the flask in the freezer overnight. The solvent was removed by cannula transfer and the solid was washed with *n*-heptane until all of the purple color was gone. After drying under vacuum for several hours, the product was obtained as needle-shaped crystals (0.15 g, yield 52%). The compound was identified by comparison to literature data[43]. ^{13}C NMR (C_6D_6): δ 151.01. IR: ν_{CO} 2127, 2171 cm^{-1}.

Theoretical procedures

All quantum chemical calculations were carried out using ORCA version 4.0.1[44]. Geometries of the molecule and its fragments were optimized using density functional theory (DFT) at the ωB97X-D3 level of theory[45,46] using the ma-def2-TZVP basis set[47,48]. The ωB97X-D3 range-separated hybrid functional was used as it reduced, relative to other functionals, the self-interaction error that led to unbound electrons for the *cis*-$Pt(CO)_2Cl_2$ anion. Vibrational frequencies of all molecules and fragments were calculated to confirm that all structures were stationary points on the potential energy surface and to yield zero-point vibrational energy contributions for all fragments as well as the thermal energy (vibrational and rotational) at room temperature of the neutral molecule. High-level DLPNO-CCSD(T)[49–52] energies were calculated on the ωB97X-D3-optimized geometries using a large and diffuse aug-cc-pVQZ basis set[53–55] (aug-cc-pVQZ-PP basis set and associated pseudopotential for Pt)[56]. Reported thermochemical thresholds are at the ωB97X-D3/ma-def2-TZVP and DLPNO-CCSD(T)/aug-cc-pVQZ level of theory; all thresholds include zero-point vibrational energies for all fragments (ωB97X-D3/ma-def2-TZVP level of theory) and the thermal energy of the neutral at 85ºC (ωB97X-D3/ma-def2-TZVP level of theory). Vertical anion states of the molecule were calculated using a ΔSCF approach at the ωB97X-D3 level (i.e. the self-consistent field equations converged for each anion state). Time-dependent DFT (TDDFT) at the same level of theory was used to calculate the relaxed excited anion state. Due to root-flipping problems, this was only successful at the PBE0 level of theory[57–59].

Results and Discussion

Figure 1 shows the ion yield curves for the anions formed by DEA to *cis*-$Pt(CO)_2Cl_2$ in the energy range from about 0-10 eV and Figure 2 shows an electron ionization mass spectrum of *cis*-$Pt(CO)_2Cl_2$ recorded at 70 eV electron impact energy. In both cases, the efficiency of each fragmentation channel is reported as apparent cross section. These are derived for the negative ions by calibrating count rates with respect to the well-established cross section for SF_6^- formation from SF_6 at 0 eV incident electron energy[41]. For the positive ion spectra, count rates are calibrated with respect to the electron ionization cross section for argon at 70 eV[60]. These cross sections are not absolute and should be taken as an estimate for the lower limit of the actual cross sections. One reason for these to appear lower than the actual cross section is the possible kinetic energy release in the respective dissociation processes. Due to the low extraction field (<1Vcm^{-1}) in the ionization region of the instrument and the finite size of the entrance aperture to the

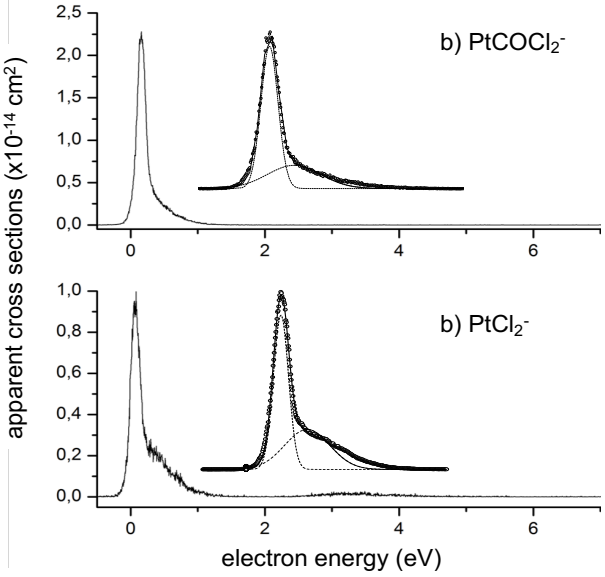

Figure 1 - Negative ion yields for loss of one and two CO ligands: a) loss of one CO ligand; b) loss of two CO ligands. The inset shows a zoom-in at 0 to 2 eV incident electron energy with Gaussian fits.

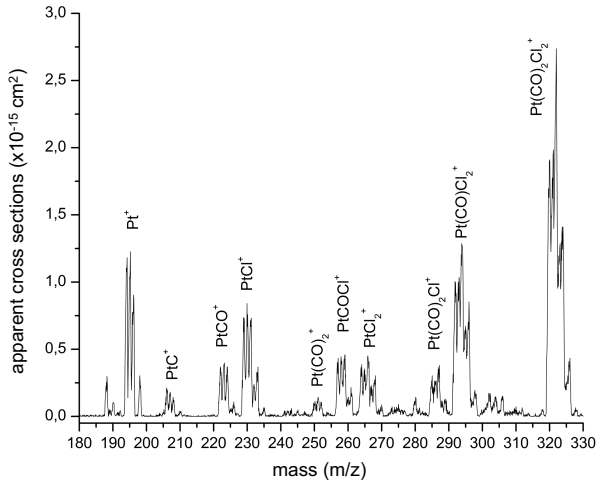

Figure 2 - Electron ionization mass spectrum recorded at 70 eV electron energy.

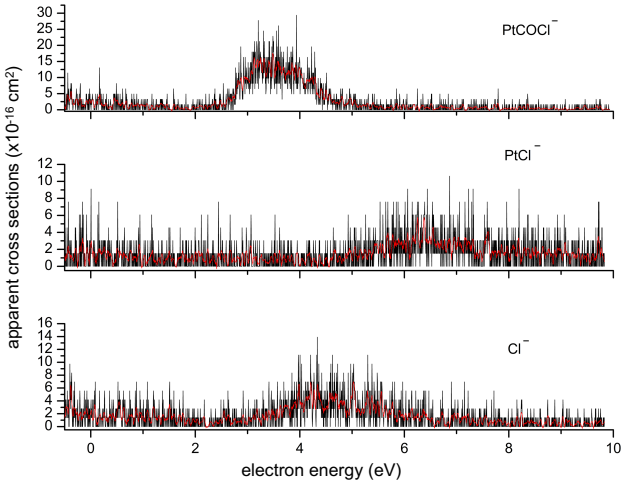

Figure 3 - Negative ion yields as function of energy for minor observed anionic fragments: $[PtCOCl]^-$ (top), $[PtCl]^-$ (middle), and Cl^- (bottom).

quadrupole, the collection efficiency of ionic fragments that are released with considerable kinetic energy may be lower than that of the molecular/atomic ions used in the cross section calibration. This will mainly affect lighter fragments. Another significant effect may result from the mass dependence of the transmission and detection efficiency of the quadrupole mass spectrometer. The current mass spectrometer is equipped with an RF generator optimised for the mass range from about 10 to 1000 amu; we thus do not expect significant influence in the relevant *m/z* mass range. Finally, the cross sections are normalized with respect to the pressure, rendering them subject to additional inaccuracies through the different ionization efficiencies of the calibration gases and the sample gas at the ion gauge. Nonetheless, these values give a better picture of the absolute efficiencies of the relevant processes than the commonly reported counts/second and may be used as lower limits to substitute generic cross sections currently used in simulations of FEBID processes.

From Figure 1, it is clear that the two most efficient DEA processes are the loss of a single CO ligand, producing $[Pt(CO)Cl_2]^-$, and the loss of two CO ligands, producing $[PtCl_2]^-$, close to 0 eV incident electron energy. The calculated threshold energies (see Table 1) are -1.78 eV and -0.48 eV, respectively at the DLPNO-CCSD(T) level of theory.

The appearance energies (AE) (reported in Table 1) for the higher energy processes are estimated using linear extrapolation from the rising edge of the respective ion yield energy curves. These are all low intensity signals and we estimate the accuracy to be approximately ±0.5 eV. Chlorine loss during DEA to $Pt(CO)_2Cl_2$, is negligible and only appears through very low intensity contributions from $[Pt(CO)Cl]^-$, $[PtCl]^-$ and Cl^- at around 3-7 eV (Fig. 3). For these three dissociation pathways the calculated thresholds are 0.19 eV, 4.11 eV and -0.51 eV, respectively. In principle the formation of Cl^- and $[Pt(CO)Cl]^-$ should thus be energetically possible through the low energy resonances. There are some minor Cl^- contributions at around 1 eV, however, the formation of these fragments is essentially observed, with low intensities, through broad high-energy contributions centered around 4.5 and 3.5 eV, respectively. Based on the width, the low intensity and the high energy, we attribute these contributions to short-lived core excited shape resonances, i.e., higher lying TNI states. The reason for these contributions not to be observed through the low energy resonances may in part be due to the unfavorable energetics as compared to single and double CO loss. However, at least for the Cl^-, where we would expect a direct dissociation from a repulsive state, the dynamics of the process and the coupling of the respective electronic states must also play a role. Pt Cl^- is also observed through a broad low intensity contribution with an onset at around 5 eV, i.e., above the calculated threshold as expected. Similar to the high energy Cl^- and $[Pt(CO)Cl]^-$ contributions, we attribute this contribution to a short lived core excited shape resonance. The apparent cross sections for these channels are more than three orders of magnitude lower than those for the CO loss. This is initially surprising as the high electron affinity of chlorine (3.6 eV[60]) makes it generally a good leaving group in DEA, and in chlorinated aliphatic and aromatic compounds Cl^- is generally the dominant negative ion fragment formed (see e.g., references [61–63] and literature therein).

To aid the interpretation of the current data we have thus calculated the thermochemical thresholds for the formation of Cl^-, $[Cl_2]^-$, $[Pt(CO)_2Cl]^-$ and $Pt(CO)_2$, at the DLPNO-CCSD(T)/aug-cc-pVQZ level of theory, along with those for single and double CO loss, and the electron affinities for the corresponding neutral fragments. These values are shown in Table 1.

Table 1 Experimental appearance energies and calculated DEA thresholds and electron affinities for the corresponding neutral fragments at the DLPNO-CCSD(T)/aug-cc-pVQZ and ωB97X/ma-def2-TZVP level of theory. Threshold energies include the thermal energy (0.302 eV) of the neutral at 120^{0}C.

Fragment	Appearance energy (eV)	Threshold energy (eV)		Electron affinity of the neutral (eV)	
		DLPNO-CCSD(T)	ωB97X	DLPNO-CCSD(T)	ωB97X
Cl^-	3.5	-0.51	-0.75	3.60	3.61

Cl_2^-	-	0.12	-0.23	2.46	2.53
$[PtCl]^-$	5.0	4.11	3.98	2.61	2.46
$[PtCl_2]^-$	0.0	-0.48	-0.66	4.49	4.60
$[Pt(CO)Cl]^-$	2.5	0.19	0.14	3.95	3.69
$[Pt(CO)Cl_2]^-$	0.0	-1.78	-1.93	3.37	3.44
$[Pt(CO)_2]^-$	-	4.27	4.01	0.71	0.78
$[Pt(CO)_2Cl]^-$	-	0.01	-0.18	3.08	3.07
$[Pt(CO)_2Cl_2]^-$	-	-2.05	-2.25	1.75	1.95

The loss of one and two CO moieties in DEA is found to be exothermic and in each case the ion yield (of $[Pt(CO)Cl_2]^-$ and $[PtCl_2]^-$, respectively) is characterized by a narrow contribution close to 0 eV. A broader overlapping contribution peaking close to 0.3 eV is also apparent in these ion yield curves, as signified by the Gaussian fits shown in the insets in Figure 1. From the Gaussian fits, we estimate that single CO loss (producing $[Pt(CO)Cl_2]^-$) through the 0.3 eV contribution is about 65% as intense as the single CO loss contribution at 0 eV. Similarly, we estimate that the loss of two CO through the 0.3 eV contribution (producing $[PtCl_2]^-$) amounts to about 77% of the ion yield for the loss of two CO through the 0 eV contribution.

The anionic ground state is well described as the attached electron occupying the LUMO of the neutral, which we find to be a π^* CO orbital (with Pt $5d_{xz}$ π antibonding character). Correspondingly, the first excited anionic state is well described as occupation of the LUMO+1 of the neutral, which we find to be the Pt d_{x2-y2} orbital with σ^* Pt-L character (with L= CO or L=Cl) (Figure 4).

Vertical attachment energies (VAE) for these first two excited anionic states and the adiabatic electron affinity (EA_{ad}) of $PtCl_2(CO)_2$ were calculated. The VAE describes the energy difference between the ground state neutral and anionic states resulting from the respective transition at the fixed equilibrium geometry of the neutral state.

The VAE associated with the anion ground state was calculated to be -0.91 eV at the DLPNO-CCSD(T) level of theory (−1.05 eV with ωB97X-D3) and the adiabatic electron affinity is found to be 1.75 eV (1.95 eV with ωB97X-D3). The VAE for the first excited anion state (occupation of LUMO+1) was calculated using a delta-SCF approach, only at the ωB97X-D3 level of theory and was found to be −0.67 eV. Hence, the VAEs associated with formation of the ground-state and first excited state anions are both negative at the equilibrium geometry of the neutral molecule. Both these states are anti-boding and as can be seen from Fig. 5, they are both associated with a considerable bond elongation along the respective dissociation coordinates. The slope of the potential energy curve at nuclear distances shorter than the equilibrium distance is always negative. Thus, in a quasi-diatomic model depicted along the respective reaction coordinates, the negative VAE and the observation of negative ions from these states, necessitates that the potential energy curves of both anionic states cross the ground state vibrational level of the neutral at nuclear distances shorter than the respective neutral equilibrium distances. In this context, we note that the relaxation of the ground state anion is associated with an out-of-plane bending mode of the CO ligand, where the dihedral Pt-CO angle changes from ~180° in the neutral to ~140° in the relaxed anion. On the other hand, the first excited state (calculated by a TDDFT approach) retains the planar geometry, but as stated above both the Pt-Cl and Pt-CO bonds are significantly elongated (Figure 5).

Within a quasi-diatomic model, we anticipate that the 0 eV contribution in the current ion yields reflects electron attachment to the π^* CO orbital with the highest transition probability at about 0 eV, where the anionic potential energy curve crosses the ground state vibrational level of the neutral. The contribution peaking at around 0.3 eV is otherwise attributed to direct attachment to the excited anion state (with σ^* Pt-L character), with a maximum transition probability at higher energy. Here, dissociation from the σ^* Pt-L is direct and the favourable channel is the exothermic CO loss (threshold of −1.78 eV), while the endothermic Cl loss (threshold of +0.01 eV) is not observed. Effective dissociation from the ground anion state (electron occupying a π^* CO with Pt $5d_{xz}$ π^* antibonding character) along the same path, on the other hand, is in principle symmetry forbidden and requires effective coupling of the occupied CO π^* orbital with the respective σ^* Pt-L LUMO+1. We anticipate that such effective coupling is provided by the out of plane bending of the CO group, analogous to what has been

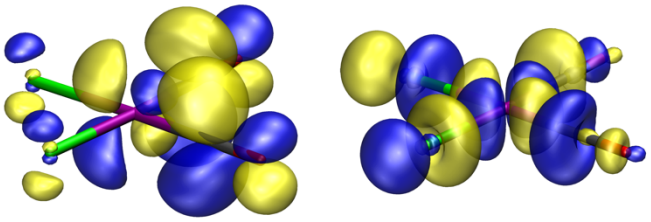

Figure 4 - Left: The SOMO for the anion ground state. Right: The SOMO for the 1st excited state of the anion.

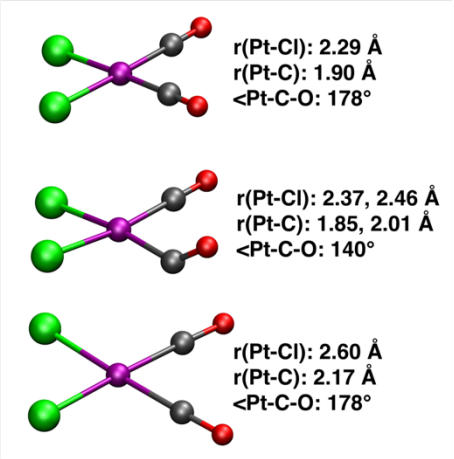

Figure 5 - Geometries of the neutral ground state (top), the anion ground state (middle) and the 1st excited state (bottom; from a PBE0-TDDFT optimization). Angles are in degrees and bond lengths in angstrom. Purple Pt; grey C; green Cl and red O.

shown for e.g. acetylene[64,65], methyl and dimethylacetylene[66], chloroethylene and chlorofluoroethylene[67], vinyl and allyl chloride, chlorobenzene and benzylchloride[68].

In addition to the low-energy contributions, the loss of two CO to produce $[PtCl_2]^-$ is also observed through a higher-lying resonance appearing through a contribution peaking around 3.5 eV in the respective ion yield curve. Single CO loss, producing $[Pt(CO)Cl_2]^-$, is not observed to have this higher-energy contribution; we attribute this to the excess energy available for further dissociation. In the current experimental setup, the extraction time from the ionization region is about 10 µs while the flight time through the quadrupole is about 50 µs. Ions that fragment during the flight through the quadrupole mass filter will not maintain stable trajectories and thus will not be detected. The currently observed ions are thus those that fragment during the first 10 µs and are stable during the flight through the mass filter. It is clear from Table 1 and the significant 0 eV contribution to the $[Pt(CO)Cl_2]^-$ ion yield that the single CO loss is an exothermic process. At the DLPNO-CCSD(T) level of theory we find this process to be exothermic by 1.78 eV. At the onset of the high energy resonance, which appears above 2 eV in the $[PtCl_2]^-$ ion yield, the excess energy in the $[Pt(CO)Cl_2]^-$ fragment (i.e., after the first CO loss) is therefore close to or even above 3.5 eV (depending also on the kinetic energy release (KER) in the process). Hence, the survival probability of $[Pt(CO)Cl_2]^-$ is low at this energy and further decomposition to $[PtCl_2]^-$ is the predominant process.

Other fragments are also formed upon electron attachment, but with relative intensities three orders of magnitude lower than these observed for the loss of one and two CO ligands. The ion yields for these fragments: $[Pt(CO)Cl]^-$, $[PtCl]^-$, and Cl^-, are shown in Figure 3. The reactions leading to the formation of $[Pt(CO)Cl]^-$ and $[PtCl]^-$ are endothermic by 0.19 and 4.11 eV, respectively, calculated at the DLPNO-CCSD(T) level of theory. They are only observed through low-intensity contributions from broad resonances with ion yields centred around 3.5 and 7.5 eV, respectively. The formation of Cl^-, conversely, is calculated to be exothermic by 0.51 eV, but is only observed with low intensity at around 4.5 eV (Figure 3).

Compared to the negative ion formation through DEA to $Pt(CO)_2Cl_2$, DI leads to a much more extensive fragmentation. Figure 2 shows the positive ion mass spectrum recorded at 70 eV incident electron energy. This energy is well above the ionization threshold of the parent molecule, so all fragmentation channels are energetically accessible.

In Table 2, estimated cross sections for the cationic observed species are summarised. Although the dominant contribution is from the parent cation with an apparent cross section of ~8.15 × 10^{-15} cm^2, the bare Pt^+ ion is also observed with considerable intensity. Indeed, it is comparable to the intensity of the contribution from single CO loss, $[Pt(CO)Cl_2]^+$ (~3.80 × 10^{-15} cm^2). Furthermore, the apparent cross sections for the formation of fragments that have lost one or both chlorine atoms ($[PtCO]^+$, $[Pt(CO)Cl]^+$ and $[Pt(CO)_2Cl]^+$) are in the range from about 0.7-1.2 × 10^{-15} cm^2, which is comparable to the cross section for $[PtCl_2]^+$, i.e., the loss of two CO ligands. The loss of both CO ligands together with chlorine, producing $[PtCl]^+$, is also observed with appreciable intensity (~1.91 × 10^{-15} cm^2). Finally, the loss of both chlorines ($[Pt(CO)_2]^+$) and the formation of platinum carbide, $[PtC]^+$, are also observed, both with apparent cross sections of about 0.3 × 10^{-15} cm^2.

Table 2 Estimated cross sections for the observed cationic species upon 70 eV electron ionization

Cation	***Cross sections*** *(× 10^{-15} cm^2)*
$Pt(CO)_2Cl_2^+$	8.15
$Pt(CO)Cl_2^+$	3.80
Pt^+	2.22
$PtCl^+$	1.91
$Pt(CO)Cl^+$	1.14
$PtCl_2^+$	1.11
$Pt(CO)_2Cl^+$	0.83
$Pt(CO)^+$	0.79
PtC^+	0.32
$Pt(CO)_2^+$	0.25

To offer some comparison of the efficiency of chlorine vs carbonyl loss through DEA and DI, we have estimated the average CO and Cl loss per incident in both cases. For the DEA process, the average CO loss was obtained by integrating the energy dependence profile for the respective fragments (loss of one and two CO). The individual contributions were then weighted by the number of carbonyls lost and divided by the sum over both channels. Since the values for minor fragments are negligible in DEA, those were not taken into consideration. For DI, the fragment peaks from the mass spectrum were integrated and individually weighted by the number of chlorine or carbonyl ligands lost. From these calculations, we derive an average CO loss of 1.4 per dissociation incident through the DEA process, while the Cl loss through DEA is considered negligible. For the DI process, we derive values of 0.6 CO ligands lost per dissociation incident and 0.5 Cl ligands lost per dissociation incident. Hence, while DEA leads almost exclusively to CO loss and no formation of the bare Pt ion is observed, the CO and Cl loss are comparably effective in DI and the formation of the bare Pt ion is significant.

As discussed in the introduction, Spencer *et al.* [69,70] have reported two surface studies on electron-induced decomposition of $Pt(CO)_2Cl_2$ under controlled UHV conditions. In the first[69], they studied the electron-induced decomposition of 1-2 monolayers of $Pt(CO)_2Cl_2$ sublimed at 80ºC and deposited on the cooled surface at about -90ºC. The deposits were exposed to 500 eV electrons from a flood gun and changes in the deposit composition were monitored with XPS and desorption from the surface with mass spectrometry. In the latter study[70], deposits of an estimated thickness of > 200 nm were created in an Auger spectrometer at room temperature with continuous precursor supply during 10 keV electron exposure, i.e., under quasi-steady state conditions. The deposits were then studied with respect to post-deposition purification by means of atomic hydrogen and extended electron exposure. Auger electron spectroscopy and energy-

dispersive X-ray analyser (EDS) were used for composition analysis.

In the non-steady state experiments on a few monolayers of adsorbed $Pt(CO)_2Cl_2$, an initial step of effective CO desorption is observed up to an electron dose of about 10^{16} e^-/cm^2, while essentially no Cl loss is observed in this electron dose range. This is reflected in the MS, where significant CO, but only marginal Cl desorption is observed. Accordingly, XPS reveals an average loss of 1-2 CO ligands per molecule from the surface but no noticeable reduction in the chlorine content with these electron doses. Prolonged electron exposure, up to about 10^{19} e^-/cm^2, then leads to virtually complete Cl removal. Similarly, the deposits formed under quasi-steady state conditions in the Auger spectrometer were found to be composed of $PtCl_2$ with no noticeable residual contamination from the CO ligands. Extended post-deposition electron exposure (>10^{17} e^-/cm^2) then led to effective Cl removal from the surface layers of the deposit, but the bulk composition stayed unchanged at a Pt:Cl ratio of 1:2. Hence, the initial deposition step is dominated by efficient CO loss leading to the formation of a $PtCl_2$ deposit. Electron-stimulated chlorine desorption from the $PtCl_2$ deposit may then be achieved with further extended electron exposure; however, the chlorine desorption in this process is limited to the first few surface layers. The current gas phase experiments are conducted under single collision conditions and can thus only be compared to the first step in the surface experiments and provide no information on the low energy electron interaction with $PtCl_2$ leading to electron induced post-deposition removal of the chlorine.

In general, one would expect the low energy secondary electron-induced processes in FEBID to constitute a convolution of the energy dependence of the individual processes (DEA, DI, ND and DD) over the energy distribution of the secondary electrons. Considering the data presented here, the DI cross sections at 70 eV are only half that DEA cross sections at peak intensities. However, while DEA only proceeds in a very narrow energy range, the integral cross sections for the DI process stretch from the onset of the respective process to very high electron energies. Thus, when comparing these processes one has to consider the effective damage yield as discusses in detail in Ref. [22]. Though we cannot state any absolute values for this, the secondary electron yield is known to be significant in the relevant DI energy range from about 10 to 100 eV. It is thus surprising that chlorine desorption is fully absent in the surface experiments.

In addition, the surface experiments were conducted on different surfaces (including on $PtCl_2$), under none-steady state conditions at about -90ºC and under quasi-steady state conditions at room temperature, with no noticeable chlorine loss (initial step in the none-steady state experiments). This could be taken as an indication that the DEA process (or eventually ND), rather than the DI process, is dominant in the surface experiments. However, the bulk of the total apparent DI cross section reported here for chlorine loss is from fragments that have also lost one or both carbonyl groups. In a metastable decay process from the molecular ion, the surface would offer an effective path for energy dissipation that may inhibit ligand loss. In this context, we note that the ion extraction time in our experiment is about 10 μs, which is ample time for metastable decay. As the generally favoured dissociation paths in metastable decay are those of the lowest binding energy ligands, the loss of one or both CO units before chlorine loss in DI may be the preferable path leading to the observation of the dominant chlorine loss fragments in the gas phase, i.e. sequential ligand loss where the CO ligands dissociate from the molecular ion before the chlorine ligands. Due to efficient energy dissipation at the surface, such metastable decay may halt after the loss of one or two CO units at the surfaces and thus quench the chlorine loss, rather than the CO loss, in the DI process. The DEA process, on the other hand, constitutes a direct dissociation along the Pt-CO reaction coordinate and at the DLPNO-CCSD(T) level of theory we find the VAE to be -0.91 eV and the dissociation limit (the threshold energy of CO loss) is −1.78 eV. The attachment energy of the parent molecule is found to be 2.05 eV, only 0.27 eV below the dissociation limit. This is thus a highly exothermic process along a steep potential energy surface and the energy minimum for the relaxed molecular anion is shallow. For neutral dissociation through electronic excitation, we anticipate a similar situation for the lowest lying anti-bonding states as the initial electron excitation constitutes a transition from a bonding/non-bonding orbital to the same antibonding orbitals that are occupied by the incoming electron in the DEA process.

These considerations rationalize the lack of chlorine desorption in the surface and desorption experiments as being the result of individual dissociation channels being quenched, rather than being due to a specific dissociation mechanism dominating the decomposition at surfaces, i.e. DEA, ND or DI. Moreover, experiments in electron-induced fragmentation of pure clusters of $Fe(CO)_5$ and its clusters deposited in Ar nanoparticles[12,71], where the energy dissipation is efficient, have shown the quenching of fragmentation pathways when compared with DEA and DI gas phase experiments under single collision conditions. Similar experiments with the current precursor may help to clarify the observations made at surfaces as compared to those made here under single collision conditions in the gas phase.

Conclusions

In the present study, we have explored dissociative electron attachment and dissociative ionization processes initiated by interaction of low-energy electrons with *cis*-$Pt(CO)_2Cl_2$. The DEA results show that the preferred fragmentation pathway is the loss of one and two carbonyl ligands, in contrast with the minor channels leading to the loss of one halogen ligand. This is distinct from the DI process, which results in a much richer fragmentation pattern. The most intense cation fragment is the parent cation (see Table 2), followed by the bare Pt cation. Moreover, Cl loss is comparable in intensity to CO loss in DI.

The dominant DEA mechanism is explained in terms of two low energy resonances, leading to the incoming electron occupying the LUMO and LUMO+1 of the neutral molecule, respectively. The former is of metal d to π* CO back bonding character and

the latter of σ* Pt-L (L=Cl or L=CO) character. The anionic states are both strongly repulsive, and the predominant CO dissociation is attributed to the lower bond dissociation energy of the platinum-carbonyl bond *vs* the platinum-chloride bond.

The DI mechanism, on the other hand, is interpreted as consisting primarily of metastable decay of the initially formed parent ion. The excess energy then leads to sequential ligand loss with the loss of the weaker bound CO ligands dominating the initial fragmentation in this process.

Previous surface studies[38] have reported that chlorine desorption from the surface was not detected during the initial deposition regime. This is consistent with the efficient energy dissipation at surfaces preferably quenching the slower Cl loss as compared to the CO loss in metastable decay in DI, while not strongly influencing the CO loss from strongly repulsive states formed in DEA. Hence, we anticipate that the efficiency of the quenching of the individual channels depends on the respective dissociation dynamics, rather than the initial ionization or excitation mechanism.

The findings reported in this paper show the important role of low-energy electron interactions in the deposition of metals from organometallic precursors in FEBID, which emphasizes their importance in the design of new precursors for FEBID.

Conflicts of interest

There are no conflicts to declare.

Acknowledgements

This work has been supported by the Icelandic Center of Research (RANNIS), Grant No. 13049305(1-3) and the University of Iceland Research Fund and was conducted within the framework of ELENA, a European Union's Horizon 2020 research and innovation programme under the Marie Skłodowska-Curie grant agreement No 722149. FFS acknowledges the Portuguese National Funding Agency FCT-MCTES through researcher position IF-FCT IF/00380/2014, and the research grants UID/FIS/00068/2019 and PTDC/FIS-AQM/31215/2017. FFS also acknowledges CELINA COST ACTION for the STSM to the visit to the laboratory at the University of Iceland. LMW thanks the US National Science Foundation for support under grants CHE-1607547 and CHE-1904802.

Notes and references

1 I. Utke, P. Hoffmann and J. Melngailis, *J. Vac. Sci. Technol. B Microelectron. Nanom. Struct.*, 2008, **26**, 1197.

2 W. F. van Dorp and C. W. Hagen, *J. Appl. Phys.*, 2008, **104**, 081301.

3 M. Huth, F. Porrati, C. Schwalb, M. Winhold, R. Sachser, M. Dukic, J. Adams and G. Fantner, *Beilstein J. Nanotechnol.*, 2012, **3**, 597–619.

4 M. Allan, *J. Chem. Phys.*, 2011, **134**, 204309.

5 M. Allan, M. Lacko, P. Papp, Matejčík, M. Zlatar, I. I. Fabrikant, J. Kočišek and J. Fedor, *Phys. Chem. Chem. Phys.*, 2018, **20**, 11692–11701.

6 J. M. Khreis, J. Ameixa, F. Ferreira da Silva and S. Denifl, *Beilstein J. Nanotechnol.*, 2017, **8**, 2583–2590.

7 K. Wnorowski, M. Stano, W. Barszczewska, A. Jówko and S. Matejčík, *Int. J. Mass Spectrom.*, 2012, **314**, 42–48.

8 K. Wnorowski, M. Stano, C. Matias, S. Denifl, W. Barszczewska and Š. Matejčík, *Rapid Commun. Mass Spectrom.*, 2012, **26**, 2093–2098.

9 S. Indrajith, P. Rousseau, B. A. Huber, C. Nicolafrancesco, A. Domaracka, K. Grygoryeva, P. Nag, B. Sedmidubská, J. Fedor and J. Kočišek, *J. Phys. Chem. C*, 2019, **123**, 10639–10645.

10 M. Zlatar, M. Allan and J. Fedor, *J. Phys. Chem. C*, 2016, **120**, 10667–10674.

11 J. Lengyel, J. Kočišek, M. Fárník and J. Fedor, *J. Phys. Chem. C*, 2016, **120**, 7397–7402.

12 J. Lengyel, P. Papp, Š. Matejčík, J. Kočišek, M. Fárník and J. Fedor, *Beilstein J. Nanotechnol.*, 2017, **8**, 2200–2207.

13 S. Engmann, B. Ómarsson, M. Lacko, M. Stano, Š. Matejčík and O. Ingólfsson, *J. Chem. Phys.*, 2013, **138**, 234309.

14 S. Engmann, M. Stano, Š. Matejčík and O. Ingólfsson, *Phys. Chem. Chem. Phys.*, 2012, **14**, 14611.

15 S. Engmann, M. Stano, P. Papp, M. J. Brunger, Š. Matejčík and O. Ingólfsson, *J. Chem. Phys.*, 2013, **138**, 044305.

16 J. Kopyra, P. Maciejewska and J. Maljković, *Beilstein J. Nanotechnol.*, 2017, **8**, 2257–2263.

17 J. Kopyra, F. Rabilloud and H. Abdoul-Carime, *Phys. Chem. Chem. Phys.*, 2018, **20**, 7746–7753.

18 M. Lacko, P. Papp, K. Wnorowski and Š. Matejčík, *Eur. Phys. J. D*, 2015, **69**, 84.

19 O. May, D. Kubala and M. Allan, *Phys. Chem. Chem. Phys.*, 2012, **14**, 2979–2982.

20 M. Neustetter, F. Ferreira da Silva and S. Denifl, *Rapid Commun. Mass Spectrom.*, 2016, **30**, 1139–1144.

21 D. H. Fairbrother, S. G. Rosenberg, C. W. Hagen, I. Utke and P. Swiderek, in *Low-energy electrons: Fundamentals and appliations*, ed. O. Ingólfsson, Pan Stanford Publishing Pte. Ltd., Singapore, 2019, pp. 219–284.

22 R. M. Thorman, T. P. Ragesh Kumar, D. H. Fairbrother and O. Ingólfsson, *Beilstein J. Nanotechnol.*, 2015, **6**, 1904–1926.

23 K. Ahlenhoff, C. Preischl, P. Swiderek and H. Marbach, *J. Phys. Chem. C*, 2018, **122**, 26658–26670.

24 O. Ingólfsson, in *Low-energy electrons Fundamentals and applications*, ed. O. Ingólfsson, Pan Stanford Publishing Pte. Ltd., Singapore, 2019, pp. 47–120.

25 J. A. Spencer, S. G. Rosenberg, M. Barclay, Y. C. Wu, L. McElwee-White and D. Howard Fairbrother, *Appl. Phys. A Mater. Sci. Process.*, 2014, **117**, 1631–1644.

26 W. G. Carden, H. Lu, J. A. Spencer, D. H. Fairbrother and L. McElwee-White, *MRS Commun.*, 2018, **8**, 343–357.

27 H. D. Fairbrother, S. G. Rosenberg, C. W. Hagen, I. Utke and P. Swiderek, in *Low-energy electrons: Fundamentals and appliations*, ed. O. Ingólfsson, Pan Stanford Publshing Pte. Ltd., Singapore, 2019, pp. 219–284.

28 S. Engmann, M. Stano, Š. Matejčík and O. Ingólfsson, *Angew. Chemie - Int. Ed.*, 2011, **50**, 9475–9477.

29 K. Landheer, S. G. Rosenberg, L. Bernau, P. Swiderek, I. Utke, C. W. Hagen and D. H. Fairbrother, *J. Phys. Chem. C*, 2011, **115**, 17452–17463.
30 S. G. Rosenberg, M. Barclay and D. H. Fairbrother, *J. Phys. Chem. C*, 2013, **117**, 16053–16064.
31 M. N. Hedhili, J. H. Bredehöft and P. Swiderek, *J. Phys. Chem. C*, 2009, **113**, 13282–13286.
32 J. D. Wnuk, J. M. Gorham, S. G. Rosenberg, W. F. van Dorp, T. E. Madey, C. W. Hagen and D. H. Fairbrother, *J. Phys. Chem. C*, 2009, **113**, 2487–2496.
33 M. Cipriani, R. M. Thorman, C. R. Brewer, L. McElwee-White and O. Ingólfsson, *Eur. Phys. J. D*, 2019.
34 R. M. Thorman, J. A. Brannaka, L. McElwee-White and O. Ingólfsson, *Phys. Chem. Chem. Phys.*, 2017, **19**, 13264–13271.
35 I. Unlu, J. A. Spencer, K. R. Johnson, R. M. Thorman, O. Ingólfsson, L. McElwee-White and H. D. Fairbrother, *Phys Chem Chem Phys*, 2018, **20**, 7862–7874.
36 R. M. Thorman, I. Unlu, K. Johnson, R. Bjornsson, L. McElwee-White, D. H. Howard and O. Ingolfsson, *Phys Chem Chem Phys*, 2018, **20**, 5644–5656.
37 J. A. Spencer, J. A. Brannaka, M. Barclay, L. McElwee-White and D. H. Fairbrother, *J. Phys. Chem. C*, 2015, **119**, 15349–15359.
38 J. A. Spencer, Y. C. Wu, L. McElwee-White and D. H. Fairbrother, *J. Am. Chem. Soc.*, 2016, **138**, 9172–9182.
39 R. M. Thorman, J. A. Brannaka, L. McElwee-White and O. Ingólfsson, *Phys. Chem. Chem. Phys.*, 2017, **19**, 13264–13271.
40 I. Bald, E. Illenberger and O. Ingólfsson, *Chem. Phys. Lett.*, 2007, **442**, 270–274.
41 M. Braun, S. Marienfeld, M. W. Ruf and H. Hotop, *J. Phys. B At. Mol. Opt. Phys.*, 2009, **42**, 125202.
42 F. Bagnoli, D. B. Dell'Amico, F. Calderazzo, U. Englert, F. Marchetti, G. E. Herberich, N. Pasqualetti and S. Ramello, *J. Chem. Soc. - Dalt. Trans.*, 1996, 4317–4318.
43 F. Calderazzo, *J. Organomet. Chem.*, 1990, **400**, 303–320.
44 F. Neese, *WIREs Comput Mol Sci*, 2012, **2**, 73–78.
45 J. Da Chai and M. Head-Gordon, *Phys. Chem. Chem. Phys.*, 2008, **10**, 6615–6620.
46 S. Grimme, J. Antony, S. Ehrlich and H. Krieg, *J. Chem. Phys.*, 2010, **132**, 154104.
47 F. Weigend and R. Ahlrichs, *Phys Chem Chem Phys*, 2005, **7**, 3297–3305.
48 J. Zheng, X. Xu and D. G. Truhlar, *Theor Chem Acc*, 2011, **128**, 295–305.
49 C. Riplinger and F. Neese, *J. Chem. Phys.*, 2013, **138**, 034106.
50 C. Riplinger, P. Pinski, U. Becker, E. F. Valeev and F. Neese, *J. Chem. Phys.*, 2016, **144**, 024109.
51 C. Riplinger, B. Sandhoefer, A. Hansen and F. Neese, *J. Chem. Phys.*, 2013, **139**, 134101.
52 M. Saitow, U. Becker, C. Riplinger, E. F. Valeev and F. Neese, *J. Chem. Phys.*, 2017, **146**, 164105.
53 T. H. Dunning, *J. Chem. Phys.*, 1989, **90**, 1007–1023.
54 D. E. Woon and T. H. Dunning, *J. Chem. Phys.*, 1993, **98**, 1358–1371.
55 R. A. Kendall, T. H. Dunning and R. J. Harrison, *J. Chem. Phys.*, 1992, **96**, 6796–6806.
56 D. Figgen, K. A. Peterson, M. Dolg and H. Stoll, *J. Chem. Phys.*, 2009, **130**, 164108.
57 C. Adamo, V. Barone and C. Adamo, *J. Chem. Phys.*, 1999, **110**, 6158.
58 M. Ernzerhof and G. E. Scuseria, *J. Chem. Phys.*, 1999, **110**, 5029.
59 J. P. Perdew, K. Burke and M. Ernzerhof, *Phys Rev Lett*, 1996, **77**, 3865–3868.
60 D. Rapp and P. Englander-Golden, *J. Chem. Phys.*, 1965, **43**, 1464–1479.
61 S. Denifl, S. Matejcik, B. Gstir, G. Hanel, M. Probst, P. Scheier and T. D. Märk, *J. Chem. Phys.*, 2003, **118**, 4107–4114.
62 Y. V. Vasil'ev, V. G. Voinov, D. F. Barofsky and M. L. Deinzer, *Int. J. Mass Spectrom.*, 2008, **277**, 142–150.
63 J. Kopyra, *Eur. Phys. J. D*, 2014, **68**, 202.
64 S. T. Chourou and A. E. Orel, *Phys. Rev. A - At. Mol. Opt. Phys.*, 2009, **80**, 3–4.
65 S. T. Chourou and A. E. Orel, *Phys. Rev. A - At. Mol. Opt. Phys.*, 2008, **77**, 1–10.
66 R. Janečková, O. May and J. Fedor, *Phys. Rev. A - At. Mol. Opt. Phys.*, 2012, **86**, 1–6.
67 P. D. Burrow, A. Modelli, N. S. Chu and K. D. Jordan, *Chem. Phys. Lett.*, 1981, **82**, 270.
68 K. L. Stricklett, S. C. Chu and P. D. Burrow, *Chem. Phys. Lett.*, 1986, **131**, 279–284.
69 J. A. Spencer, Y. C. Wu, L. McElwee-White and D. H. Fairbrother, *J. Am. Chem. Soc.*, 2016, **138**, 9172–9182.
70 J. A. Spencer, M. Barclay, M. J. Gallagher, R. Winkler, I. Unlu, Y. C. Wu, H. Plank, L. McElwee-White and D. H. Fairbrother, *Beilstein J. Nanotechnol.*, 2017, **8**, 2410–2424.
71 J. Lengyel, J. Fedor and M. Fárník, *J. Phys. Chem. C*, 2016, **120**, 17810–17816.